Free-boundary toroidal Alfvén eigenmodes

Eugene Y. Chen,[a] H. L. Berk, B. Breizman, and L. J. Zheng
Institute for Fusion Studies, University of Texas at Austin, 1 University Station, C1500, Austin, Texas 78714, USA

(Received 14 January 2011; accepted 16 March 2011; published online 11 May 2011)

A numerical study is presented for the $n=1$ free-boundary toroidal Alfvén eigenmodes (TAE) in tokamaks, which shows that there is considerable sensitivity of $n=1$ modes to the position of the conducting wall. An additional branch of the TAE is shown to emerge from the upper continuum as the ratio of conducting wall radius to plasma radius increases. Such phenomena arise in plasma equilibria with both circular and shaped cross sections, where the shaped profile studied here is similar to that found in Alcator C-Mod. © *2011 American Institute of Physics*.
[doi:10.1063/1.3575157]

I. INTRODUCTION

Toroidal Alfvén eigenmodes (TAE) are discrete eigenmodes which exist in the toroidicity induced frequency gaps. These modes may be readily destabilized by high energy alpha particles in ignited tokamak plasmas, resulting in degraded confinement. Therefore, the study of the TAE and their stability characteristics has attracted considerable attention.[1]

Calculations of TAE are frequently performed with fixed-boundary conditions that assume that the radial perturbation vanishes at the plasma edge.[2–13] Such calculations ignore the presence of a vacuum gap between the plasma and the ideal conducting wall, which is appropriate to localized modes that are insensitive to the outer boundary conditions. However, for modes of low toroidal mode number, it is unclear that the mentioned boundary conditions remain applicable. A more realistic set of boundary conditions are the free-boundary conditions which allow the radial component of the magnetic displacement vector ($\vec{\xi}$) to be nonzero at the plasma–vacuum interface.[14] While this set of boundary conditions has been implemented in some magnetohydrodynamics (MHD) eigenmode codes that deal with cylindrical plasma[15–17] and toroidal plasma,[18,19] a systematic investigation which explores the relation between TAE and various equilibrium/configuration parameters in the presence of them has not yet been conducted.

The present paper is intended to partially fulfill such purposes. Here, we study the sensitivity of eigenfrequency and eigenmode structure to the ratio of the conducting wall radius to plasma radius. Additional mode sensitivity scans will be presented for variable edge q (safety factor) conditions and to plasma β (the ratio of average plasma pressure to magnetic pressure, $\mu_0\langle p\rangle/\langle B^2\rangle$) variations. In this paper we refer to the modes that we study as "Free-boundary TAE."

This paper is organized as follows: In Sec. II, we introduce our numerical scheme. In Sec. III, we investigate the response of eigenfrequency and mode structure of TAE to various system parameters. In Sec. IV, we study free-boundary TAE for a plasma profile similar to that found in Alcator C-Mod. Discussions and concluding remarks are presented in Sec. V.

II. NUMERICAL SCHEME

The numerical investigations in this paper employ the ideal MHD eigenmode code AEGIS (Adaptive EiGenfunction Independent Solution).[20] The AEGIS code uses the energy principle to search for the MHD eigenvalues and eigenfunctions of an axisymmetric toroidal plasma surrounded by a vacuum gap and enclosed by a perfectly conducting wall whose shape conforms to the plasma boundary (viz., the vacuum gap is of constant width). A schematic diagram is shown in Fig. 1, where the long vertical dashed line to the left depicts the major axis of the tokamak and the long horizontal line depicts the mid-plane. We define the plasma radius (a) as the distance from the magnetic axis (indicated by the round dot inside the plasma region) to the outer mid-plane plasma edge and the wall radius (b) as the distance from the magnetic axis to the outer mid-plane conducting wall. The vacuum gap is indicated by the white area between the plasma and the wall.

In a toroidally symmetric configuration, the magnetic field $\vec{B}$ in the Princeton equilibrium and stability (PEST) coordinates[21] can be represented by the form,

$$\vec{B} = \chi'\nabla\phi \times \nabla\psi + g(\chi)\nabla\phi, \tag{1}$$

where ϕ is the axisymmetric toroidal angle, ψ labels the magnetic surface, $\chi(\psi)$ denotes the poloidal magnetic flux, and $g(\chi)$ denotes the poloidal current flux. The poloidal flux is governed by the Grad–Shafranov equation. In this work, the equation is solved by the TOQ code (https://fusion.gat.com/THEORY/toq/). The TOQ code takes the pressure profile $P(\chi)$ and poloidal current flux $g(\chi)$ as input and solves for χ as a function of position. This allows the code to solve the problem of relating the flux coordinates to the Euclidean coordinates (viz., $X(\psi,\theta)$ and $Z(\psi,\theta)$ where θ is the generalized poloidal angle, X is the distance to the major axis and Z is the distance to the mid-plane).

The numerically evaluated equilibrium is used to express the perturbed plasma potential energy and kinetic energy,

[a]Author to whom correspondence should be addressed. Electronic mail: eyc@mail.utexas.edu.

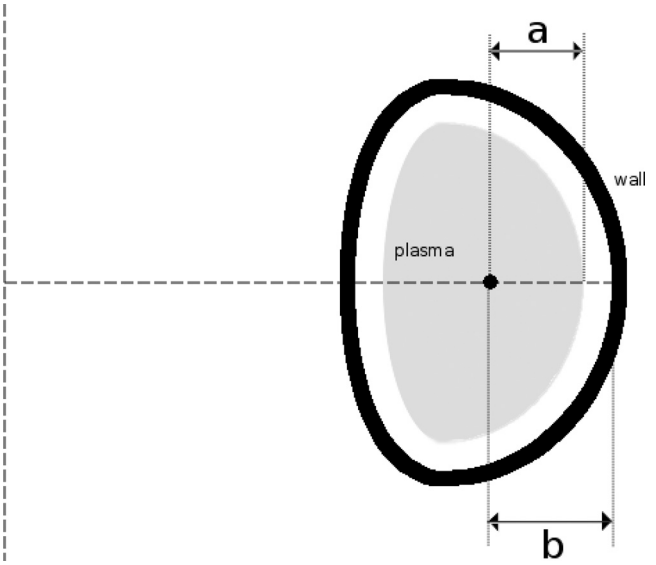

FIG. 1. Schematic diagram of the tokamak poloidal cross section.

$$\delta W_p = \frac{1}{2\mu_0}\int d\tau \left[\left|\vec{Q} + \mu_0 \frac{(\vec{\xi}\cdot\nabla\psi)\vec{J}\times\nabla\psi}{|\nabla\psi|^2}\right|^2 - 2U|\vec{\xi}\cdot\nabla\psi|^2\right] \tag{2}$$

$$\delta W_k = \frac{1}{2}\int d\tau \rho\omega^2|\vec{\xi}|^2 \equiv \omega^2 I \tag{3}$$

in which μ_0 is the permeability of free space, ω is the wave frequency, $\vec{\xi}$ is the magnetic field line displacement vector, $\vec{Q} = \nabla\times(\vec{\xi}\times\vec{B})$, $\vec{J}$ is the equilibrium current density, and I is the norm of the mode. The quantity $2U$ only depends on the MHD equilibrium and do not affect the analysis below. Its definition is given in Appendix A.

In this work we set the adiabatic index to zero, which is tantamount to ignoring acoustic compression effects. With this choice the parallel component of $\vec{\xi}$ decouples from the MHD equations while the magnetic compressibility is still included.

We decompose $\vec{\xi}$ in the following way:

$$\vec{\xi} = \xi^{\psi}\chi'\frac{\vec{B}\times\vec{s}}{B^2} + i\xi^{s}\chi'\frac{\vec{B}\times\nabla\psi}{B^2}, \tag{4}$$

where $\vec{s} = \nabla\phi - q\nabla\theta$. We further represent ξ^s as

$$\xi^s = \frac{1}{n}\frac{\partial\xi^{\psi}}{\partial\psi} + \delta \equiv \frac{1}{n}\xi^{\psi'} + \delta, \tag{5}$$

in which n is the toroidal mode number. δW_p and $\omega^2 I$ can then be put into a quadratic form for the triad of the functions $(\xi^{\psi}, \xi^{\psi'}, \delta)$. By exploiting the toroidal symmetry of the system, the radial linear perturbation ξ^{ψ} can be decomposed in the following form:

$$\xi^{\psi}(\psi) = \sum_{m=m_{\min}}^{m_{\max}} \xi^{\psi}_m(\psi)e^{i(m\theta - n\varphi)}. \tag{6}$$

We have

$$2\mu_0\delta W_p = \int d\psi(\tilde{\xi}^{\psi\dagger}\tilde{\xi}^{\psi'\dagger}\tilde{\delta}^{\dagger})\begin{pmatrix}\mathcal{A}_p & \mathcal{P}_p & \mathcal{R}_p\\ \mathcal{P}_p^{\dagger} & \mathcal{B}_p & \mathcal{Q}_p\\ \mathcal{R}_p^{\dagger} & \mathcal{Q}_p^{\dagger} & \mathcal{C}_p\end{pmatrix}\begin{pmatrix}\tilde{\xi}^{\psi}\\ \tilde{\xi}^{\psi'}\\ \tilde{\delta}\end{pmatrix}$$

$$2\mu_0\omega^2 I = \int d\psi(\tilde{\xi}^{\psi\dagger}\tilde{\xi}^{\psi'\dagger}\tilde{\delta}^{\dagger})\rho\omega^2\begin{pmatrix}\mathcal{A}_i & \mathcal{P}_i & \mathcal{R}_i\\ \mathcal{P}_i^{\dagger} & \mathcal{B}_i & \mathcal{Q}_i\\ \mathcal{R}_i^{\dagger} & \mathcal{Q}_i^{\dagger} & \mathcal{C}_i\end{pmatrix}\begin{pmatrix}\tilde{\xi}^{\psi}\\ \tilde{\xi}^{\psi'}\\ \tilde{\delta}\end{pmatrix}, \tag{7}$$

where the tilde indicates a vector in Fourier space, e.g.,

$$\tilde{\xi}^{\psi} = \begin{pmatrix}\xi^{\psi}_1\\ \xi^{\psi}_2\\ \vdots\\ \xi^{\psi}_M\end{pmatrix}. \tag{8}$$

In this representation, ξ^{ψ}_1 is the Fourier component corresponds to $m_{\min}$ and ξ^{ψ}_M corresponds to $m_{\max}$. Note that $M = m_{\max} - m_{\min} + 1$. The calligraphic letters used here denotes $M\times M$ matrices determined by the MHD equilibrium [c.f. Eqs. (2) and (3)]. We refer the readers to Appendix A for their detailed expressions. Defining

$$\begin{pmatrix}\mathcal{A} & \mathcal{P} & \mathcal{R}\\ \mathcal{P}^{\dagger} & \mathcal{B} & \mathcal{Q}\\ \mathcal{R}^{\dagger} & \mathcal{Q}^{\dagger} & \mathcal{C}\end{pmatrix} = \begin{pmatrix}\mathcal{A}_p & \mathcal{P}_p & \mathcal{R}_p\\ \mathcal{P}_p^{\dagger} & \mathcal{B}_p & \mathcal{Q}_p\\ \mathcal{R}_p^{\dagger} & \mathcal{Q}_p^{\dagger} & \mathcal{C}_p\end{pmatrix} - \rho\omega^2\begin{pmatrix}\mathcal{A}_i & \mathcal{P}_i & \mathcal{R}_i\\ \mathcal{P}_i^{\dagger} & \mathcal{B}_i & \mathcal{Q}_i\\ \mathcal{R}_i^{\dagger} & \mathcal{Q}_i^{\dagger} & \mathcal{C}_i\end{pmatrix}. \tag{9}$$

It follows that,

$$2\mu_0(\delta W_p - \omega^2 I) = \int d\psi(\tilde{\xi}^{\psi\dagger}\tilde{\xi}^{\psi'\dagger}\tilde{\delta}^{\dagger})\begin{pmatrix}\mathcal{A} & \mathcal{P} & \mathcal{R}\\ \mathcal{P}^{\dagger} & \mathcal{B} & \mathcal{Q}\\ \mathcal{R}^{\dagger} & \mathcal{Q}^{\dagger} & \mathcal{C}\end{pmatrix}\begin{pmatrix}\tilde{\xi}^{\psi}\\ \tilde{\xi}^{\psi'}\\ \tilde{\delta}\end{pmatrix}. \tag{10}$$

We then apply Euler–Lagrange equation with respect to $\delta^{\dagger}$, obtaining

$$\mathcal{R}^{\dagger}\tilde{\xi}^{\psi} + \mathcal{Q}^{\dagger}\tilde{\xi}^{\psi'} + \mathcal{C}\tilde{\delta} = 0, \tag{11}$$

$$\tilde{\delta} = (-\mathcal{C}^{-1}\mathcal{R}^{\dagger}, -\mathcal{C}^{-1}\mathcal{Q}^{\dagger})\begin{pmatrix}\tilde{\xi}^{\psi}\\ \tilde{\xi}^{\psi'}\end{pmatrix}. \tag{12}$$

Equation (10) can thus be reduced to

$$2\mu_0(\delta W_p - \omega^2 I) = \int d\psi(\tilde{\xi}^{\psi'\dagger}\tilde{\xi}^{\psi\dagger})\begin{pmatrix}\mathcal{F} & \mathcal{K}\\ \mathcal{K}^{\dagger} & \mathcal{G}\end{pmatrix}\begin{pmatrix}\tilde{\xi}^{\psi'}\\ \tilde{\xi}^{\psi}\end{pmatrix}, \tag{13}$$

in which

$$\mathcal{F} = \mathcal{B} - \mathcal{Q}\mathcal{C}^{-1}\mathcal{Q}^{\dagger}$$
$$\mathcal{K}^{\dagger} = \mathcal{P} - \mathcal{R}\mathcal{C}^{-1}\mathcal{Q}^{\dagger}.$$
$$\mathcal{G} = \mathcal{A} - \mathcal{R}\mathcal{C}^{-1}\mathcal{R}^{\dagger}$$

Applying Euler–Lagrange equation with respect to $\tilde{\xi}^{\psi\dagger}$ then yields

$$(\mathcal{F}\tilde{\xi}^{\psi'} + \mathcal{K}\tilde{\xi}^{\psi})' - \mathcal{K}^{\dagger}\tilde{\xi}^{\psi'} - \mathcal{G}\tilde{\xi}^{\psi} = 0. \tag{14}$$

The above set of equations can be transformed into the following set of first order differential equations:

$$\mathbf{u}' = \mathcal{D}\mathbf{u}$$
$$\mathcal{D} = \begin{pmatrix} -\mathcal{F}^{-1}\mathcal{K} & \mathcal{F}^{-1} \\ \mathcal{G} - \mathcal{K}^{\dagger}\mathcal{F}^{-1}\mathcal{K} & \mathcal{K}^{\dagger}\mathcal{F}^{-1} \end{pmatrix} \tag{15}$$
$$\mathbf{u} \equiv \begin{pmatrix} \mathbf{u}_1 \\ \mathbf{u}_2 \end{pmatrix} = \begin{pmatrix} \tilde{\xi}^{\psi} \\ \mathcal{F}\tilde{\xi}^{\psi'} + \mathcal{K}\tilde{\xi}^{\psi} \end{pmatrix}.$$

Then by integrating Eq. (13) by parts, it follows that for the solutions of Eq. (15) ($\mathbf{u}$),

$$2\mu_0(\delta W_p - \omega^2 I) = \mathbf{u}_1^{\dagger}\mathbf{u}_2|_{\psi=\psi_a}. \tag{16}$$

The solution space of Eq. (15) is $2M$-dimensional. However, the physical relevant solutions require regularity at the magnetic axis. Thus, M boundary conditions (i.e., $\xi_m^{\psi} \propto r^m$ at the magnetic axis) are imposed and we are left with a M-dimensional solution subspace. Any set of M independent solutions can be taken as a set of basis function and we find it convenient to make the following choice:

$${}^{l}\mathbf{u}_{1m}|_{\psi=\psi_a} = \delta_m^l. \tag{17}$$

The M independent functions $\{{}^{l}\mathbf{u} | l = 1, ..., M\}$ constitutes a complete basis and the general solution $\mathbf{u}_g$ has the following representation:

$$\mathbf{u}_g = \left({}^{1}\mathbf{u}\,{}^{2}\mathbf{u} \cdots {}^{M}\mathbf{u}\right) \begin{pmatrix} c_{p1} \\ c_{p2} \\ \vdots \\ c_{pM} \end{pmatrix}. \tag{18}$$

We define the column vector composed of $c_{p1}, c_{p2}, \cdots, c_{pM}$ to be $\mathbf{c}_p$. Equation (16) thus becomes

$$\begin{aligned} 2\mu_0\left(\delta W_p - \omega^2 I\right) &= \mathbf{c}_p^{\dagger} \begin{pmatrix} {}^{1}\mathbf{u}_{11} & {}^{2}\mathbf{u}_{11} & \cdots & {}^{M}\mathbf{u}_{11} \\ {}^{1}\mathbf{u}_{12} & {}^{2}\mathbf{u}_{12} & \cdots & {}^{M}\mathbf{u}_{12} \\ \vdots & \vdots & \ddots & \vdots \\ {}^{1}\mathbf{u}_{1M} & {}^{2}\mathbf{u}_{1M} & \cdots & {}^{M}\mathbf{u}_{1M} \end{pmatrix}^{\dagger}\Bigg|_{\psi=\psi a} \\ &\quad \times \begin{pmatrix} {}^{1}\mathbf{u}_{21} & {}^{2}\mathbf{u}_{21} & \cdots & {}^{M}\mathbf{u}_{21} \\ {}^{1}\mathbf{u}_{22} & {}^{2}\mathbf{u}_{22} & \cdots & {}^{M}\mathbf{u}_{22} \\ \vdots & \vdots & \ddots & \vdots \\ {}^{1}\mathbf{u}_{2M} & {}^{2}\mathbf{u}_{2M} & \cdots & {}^{M}\mathbf{u}_{2M} \end{pmatrix}\Bigg|_{\psi=\psi a} \mathbf{c}_p \\ &\equiv \mathbf{c}_p^{\dagger}\mathcal{U}_{p1}^{\dagger}\mathcal{U}_{p2}\mathbf{c}_p \\ &= \mathbf{c}_p^{\dagger}\mathcal{U}_{p2}\mathbf{c}_p. \end{aligned} \tag{19}$$

The last line follows because $\mathcal{U}_{p1}$ is the identity matrix due to the basis choice given by Eq. (17). Similar notation (viz., using $\mathcal{U}$ to denote the $M \times M$ solution matrix evaluated at the plasma—vacuum interface) will be used again for the analysis in the vacuum region, but with the subscript changed from p to v.

The analysis in the vacuum region is very similar to what we have presented for the plasma region, and we shall only focus on where differences occur in the treatment: A new grid (ψ_v, θ_v, ϕ) is set in the vacuum region between the plasma boundary and the wall. As there are no currents in the vacuum region, $\nabla \times \delta B = 0$. It follows that the perturbed magnetic field can be described by a scalar field φ, where $\delta B = -\nabla\varphi$.

It can be shown that the vacuum energy integral can be expressed as a quadratic form of $(\frac{\partial\tilde{\varphi}}{\partial\psi_v}, \tilde{\varphi})$,

$$\begin{aligned} 2\mu_0\delta W_v &= \int d\tau |\nabla\varphi|^2 \\ &= \int d\psi_v \left(\frac{\partial\tilde{\varphi}^{\dagger}}{\partial\psi_v}, \tilde{\varphi}^{\dagger}\right) \begin{pmatrix} \mathcal{F}_v & \mathcal{K}_v \\ \mathcal{K}_v^{\dagger} & \mathcal{G}_v \end{pmatrix} \begin{pmatrix} \frac{\partial\tilde{\varphi}}{\partial\psi_v} \\ \tilde{\varphi} \end{pmatrix} \end{aligned} \tag{20}$$

(c.f. Appendix A for definitions of $\mathcal{F}_v, \mathcal{K}_v, \mathcal{K}_v^{\dagger}$, and $\mathcal{G}_v$.) Euler–Lagrange equation then yields

$$\mathbf{v}' = \mathcal{D}_v\mathbf{v}, \tag{21}$$

in which

$$\mathbf{D}_v = \begin{pmatrix} -\mathcal{F}_v^{-1}\mathcal{K}_v & \mathcal{F}_v^{-1} \\ \mathcal{G}_v - \mathcal{K}_v^{\dagger}\mathcal{F}_v^{-1}\mathcal{K}_v & \mathcal{K}_v^{\dagger}\mathcal{F}_v^{-1} \end{pmatrix}$$
$$\mathbf{v} \equiv \begin{pmatrix} \mathbf{v}_1 \\ \mathbf{v}_2 \end{pmatrix} = \begin{pmatrix} \tilde{\varphi} \\ \mathcal{F}_v\tilde{\varphi}' + \mathcal{K}_v\tilde{\varphi} \end{pmatrix}.$$

We note that the dimension of vacuum solution space is also M, because the ideal conducting wall imposes M boundary conditions that correspond to $\vec{B} \cdot \nabla\psi_v = 0$. Namely,

$$\mathbf{v}_2(\psi_v)|_{\psi_v=\psi_b} = 0, \tag{22}$$

as $\mathbf{v}_2$ is proportional to the Fourier vector of $\delta\vec{B} \cdot \nabla\psi_v$. By performing an integration by parts and using the vanishing of its Euler–Lagrange equation as well as the aforementioned boundary conditions, we arrive at the relation,

$$2\mu_0\delta W_v = -\mathbf{c}_v^{\dagger}\mathcal{U}_{v1}^{\dagger}\mathcal{U}_{v2}\mathbf{c}_v, \tag{23}$$

where the subscript v denotes *vacuum*. At the plasma–vacuum interface, the normal component of $\delta\vec{B}$ is continuous. This free-boundary condition gives a relation between $\mathbf{c}_p$ and $\mathbf{c}_v$,

$$\mathcal{U}_{v2}\mathbf{c}_v = -i[\chi'\mathcal{T}\mathcal{K}_{\|}]_{\psi=\psi_a}\mathbf{c}_p, \tag{24}$$

where $\mathcal{K}_{\|} = (m - nq)\mathcal{I}$ and $\mathcal{T}$ is the transformation matrix between the plasma poloidal coordinate (θ_p) and vacuum poloidal coordinate (θ_v),

$$\mathcal{T}_{m_v m_p} = \frac{1}{2\pi}\int_{-\pi}^{\pi} d\theta_p e^{-im_v\theta_v} e^{im_p\theta_p}. \tag{25}$$

Thus we have

$$2\mu_0(\delta W_p + \delta W_v - \omega^2 I) = \mathbf{c}_p^\dagger \left[\mathcal{U}_{p2} - \chi'^2 \mathcal{K}_\parallel \mathcal{T}^\dagger \mathcal{U}_{v2}^{-1\dagger} \mathcal{U}_{v1}^\dagger \mathcal{T} \mathcal{K}_\parallel\right]_{\psi=\psi_a} \mathbf{c}_p \equiv \mathbf{c}_p^\dagger \hat{L} \mathbf{c}_p. \tag{26}$$

We note that with a specific MHD equilibrium, $\hat{L}$ is both a function of frequency (through $\mathcal{U}_p$) and wall position (through $\mathcal{U}_v$). The energy principle requires an arbitrary variation of LHS to vanish, leading to the following set of M equations:

$$\hat{L}\mathbf{c}_p = 0. \tag{27}$$

Nontrivial $\mathbf{c}_p$ only exists when $\mathrm{Det}(\hat{L}) = 0$. In a given system, the problem of finding global eigenmodes is, thereby, reduced to finding the root ω_0 of $\mathrm{Det}(\hat{L}) = 0$. The nontrivial eigenvector can then be constructed for the value of ω_0.

III. EIGENVALUE AND EIGENMODE SENSITIVITY TO PARAMETER VARIATION

To start our investigation with minimal complications, we begin our study with a circular poloidal cross-section equilibrium with $q_0 = 1.10$ (q_0 denotes the q value at magnetic axis) and $q_a = 2.25$ (q_a denotes the q value at $\psi = \psi_a$). β is taken to have a negligible value (5.4×10^{-4}) and the tokamak has an aspect ratio of 4. The q-profile, density profile, and Alfvén continuum profile for this equilibrium are shown in Fig. 2. In the following three subsections, we will study the changing of free-boundary TAE as the wall position, the relative plasma pressure (β) and the safety factor at plasma boundary (q_a) vary.

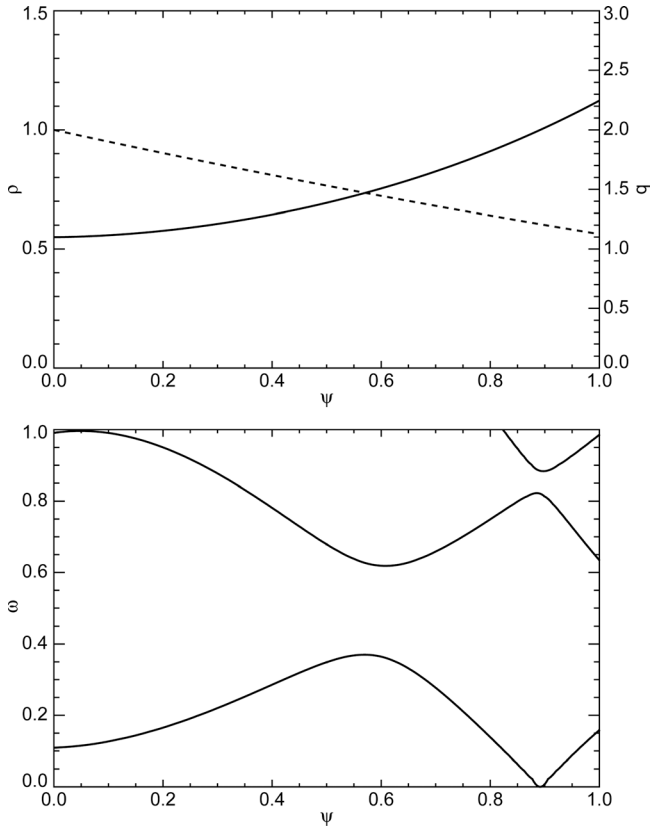

FIG. 2. Initial MHD model equilibrium parameters. Upper panel: q-profile (solid line) and density profile (dashed line). The density profile is chosen to be $\rho = (1 - D\psi)^2$, where $D = 0.25$. Lower panel: Alfvén continuum for $n = 1$.

A. Wall position study

We first explore the sensitivity of the eigenvalues and eigenmodes to the conducting wall position. We introduce the normalized wall position **b**, defined as the ratio of the wall radius to plasma radius, b/a. Thus, the value of **b** ranges from 1 to the tokamak aspect ratio (i.e., when the wall reaches the major axis). We will refer to the later limit as the "no-wall limit" because the results become very insensitive to wall position much before **b** approaches the aspect ratio, as we will see shortly. Note that because we are performing free-boundary calculation, there is a technicality that prevents **b** from being taken arbitrarily close to unity (i.e., the plasma energy becomes numerically divergent except for the eigenfunction itself). However, we have confirmed that in calculations with $\mathbf{b} = 1.001$ the mode structure expected for a fixed-boundary mode is being replicated (nearly zero radial displacement at plasma boundary). We scan for solutions, by searching in **b** rather than in ω. This enables us to precalculate the plasma contribution to the $\hat{L}$ matrix at fixed frequency inside the frequency gap, at intervals of $0.001 v_{A0}/Rq_0$ (in which v_{A0} is the Alfvén speed at the magnetic axis and R the major radius). At each frequency, we seek, using Newton's method, the wall position (**b**) by solving $\mathrm{Det}[\hat{L}(\omega; \mathbf{b})] = 0$ which then enables the construction of an eigenmode at the specified frequency. The result is summarized in Fig. 3, which plots the locus of

$$\{(\mathbf{b}, \omega) | \mathrm{Det}[\hat{L}(\omega; \mathbf{b})]\} = 0. \tag{28}$$

We see that the general trend is for the mode frequency to decrease with increasing **b**. Further, there are two different branches of the TAE as is observed in Fig. 3. The lower branch which drops into the continuum at $\mathbf{b} = 1.64$ (L2) becomes the fixed-boundary TAE at the limit of $\mathbf{b} \to 1$ (L1) (hereafter, we will refer the $\mathbf{b} \to 1$ limit as the "fixed-boundary limit"). The upper branch which is absent in the fixed-boundary limit, emerges from the upper continuum at

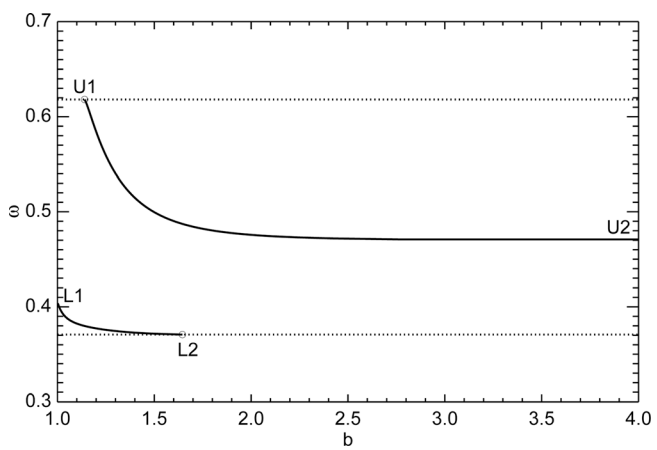

FIG. 3. The relation between wall position and eigenmode frequency for the MHD equilibrium specified by Fig. 2. The horizontal dotted lines depict the boundaries of TAE gap. U1 and L2 mark points where real frequency modes first appear.

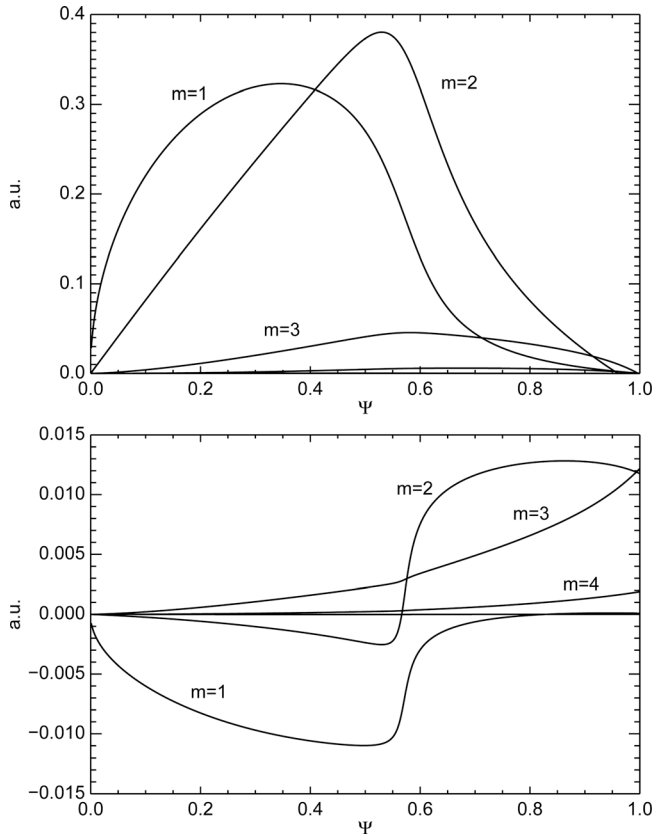

FIG. 4. Mode structure of the lower-branch free-boundary TAE in PEST coordinates. Upper panel: Structure of the lower-branch modes at the fixed-boundary limit (L1). Lower panel: Structure of the lower-branch modes at $\mathbf{b} \sim 1.64$ (L2).

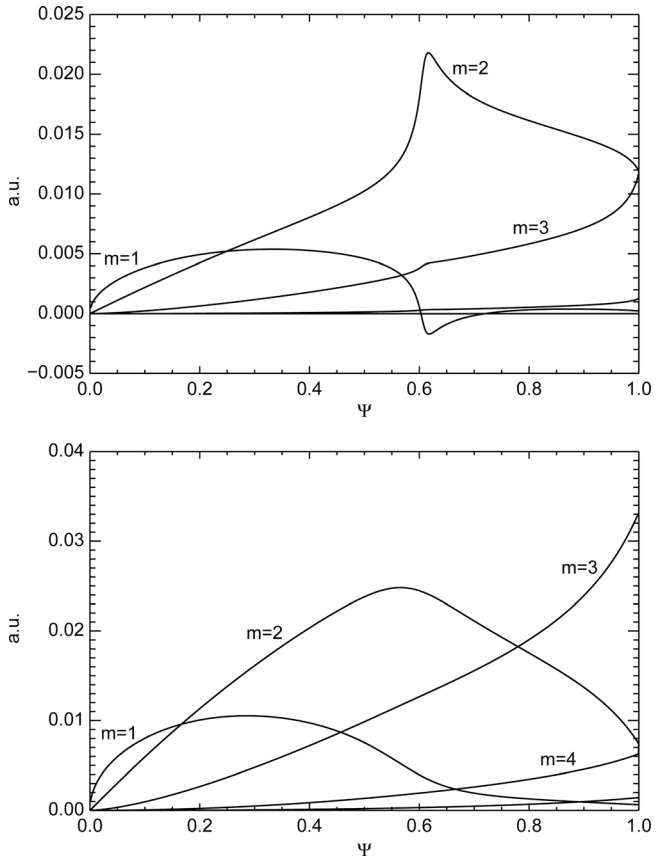

FIG. 5. Mode structure of the upper-branch free-boundary TAE in PEST coordinates. Upper panel: Structure of the upper-branch modes at $\mathbf{b} \sim 1.14$ (U1). Lower panel: Structure of the upper-branch modes at the no-wall limit (U2).

$\mathbf{b} > 1.14$ (U1). Its frequency decreases with the increase of $\mathbf{b}$ and approaches an asymptotic value of $0.47v_{A0}/R$ (U2) which nearly reached in this figure even for $\mathbf{b} \geq 2.0$.

Using PEST coordinates, we plot the structure of the lower branch free-boundary TAE in Fig. 4. The upper panel shows the mode structure at L1, whereas the lower panel shows the mode structure at L2. In the upper panel, we see that the mode has strong $m=1$ and $m=2$ components and a relatively small $m=3$ component, which is consistent with previous TAE investigations with fixed-boundary conditions (e.g., Ref. 12. Note that the radial coordinate we use in our plots are different from that used in Ref. 12; we use the normalized magnetic surface ψ/ψ_a, whereas Ref. 12 used the radial coordinate $s=\sqrt{\psi/\psi_a}$). In the lower panel (where the frequency of the mode is extremely close to the frequency tip of the lower continuum) we observe a strong $m=3$ component which is comparable to $m=2$ component at plasma edge. The mode involves three poloidal harmonics even though only one TAE gap is present in the equilibrium. It has a rather broad extent and its $m=1,2$ poloidal harmonics exhibits a pronounced in-phase jump around $q=1.5$, as is theoretically expected.[13] We shall refer this synchronism in phase as a "'couplet'" in the rest of this paper.

The mode structure of the upper-branch free-boundary TAE is shown in Fig. 5. Plotted in the upper panel is the mode structure at U1. Again, there is a strong $m=3$ component which is absent in the conventional fixed-boundary TAE. The mode frequency is very close to the tip of the upper frequency continuum, leading to the out-of-phase jumps of the $m=1,2$ couplet around $q=1.5$ as is also expected theoretically. In the lower panel, we plot the mode structure at U2 (no wall limit: $\mathbf{b}=4$). The structure of the $m=1$ and $m=2$ harmonics is not very different from the fixed-boundary TAE, consistent with the fact that the frequencies of the two modes are not very apart. However, $m=3$ is dominant at the plasma edge, and a non-negligible $m=4$ harmonic is also present.

To conclude, the structure of free-boundary TAE has features of fixed-boundary TAE, but a strong surface $m=3$ component is ubiquitous unless $\mathbf{b} \to 1$. $\mathbf{b}$, which we infer to be a major factor in shifting the mode frequency, in turn determines the mode structure of $m=1$ and $m=2$ harmonics. Furthermore, the frequency shift can cause the mode to be immersed into the continuum and disappear.

In a tokamak, the wall position is more of a fixed quantity. In this study we have found that the number and frequency of the eigenmodes in a specific equilibrium is sensitive to wall position. From Fig. 3, it can be concluded that

(1) Only one eigenmode is found for $1 < \mathbf{b} < 1.14$.
(2) Two eigenmodes are found for $1.14 < \mathbf{b} < 1.64$.
(3) Only one eigenmode is found for $\mathbf{b} > 1.64$, and this mode is not the one that evolves into the fixed-boundary TAE.

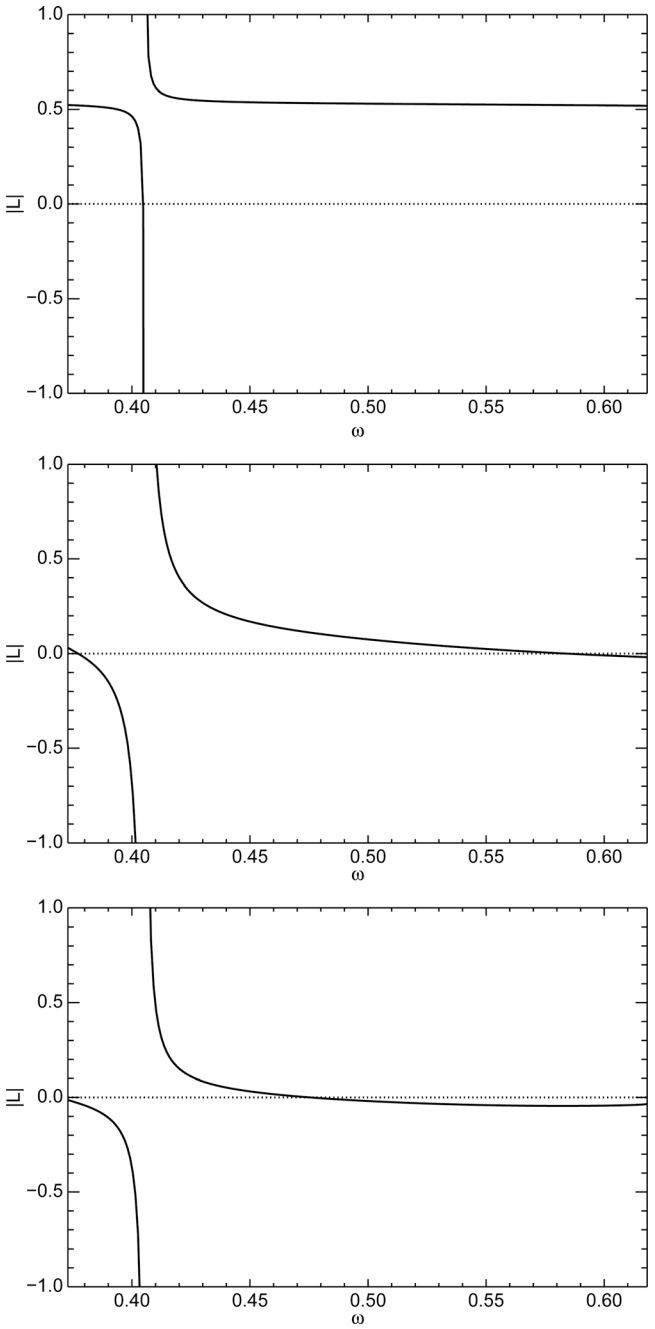

FIG. 6. Normalized $\mathrm{Det}(\hat{L})$ as a function of ω (solid line) and the horizontal line of $\mathrm{Det}(\hat{L}) = 0$ (dotted line). The intersection of the two defines a root and indicates the existence of a global eigenmode. Upper panel: $\mathbf{b} = 1.001$. Middle panel: $\mathbf{b} = 1.2$. Lower panel: $\mathbf{b} = 2.0$.

Hence, on the basis of calculation for this particular equilibrium, we see that a fixed-boundary calculation can easily make misleading predictions of the expected number of TAE which thread a gap as well as the frequency of these modes, at least as far as the $n = 1$ mode is concerned. For the purpose of illustration, we have explicitly made the eigenmode calculation for three different wall positions, viz., $\mathbf{b} = 1.001, 1.2, 2.0$. The results [$\mathrm{Det}(\hat{L})$ as a function of ω, fixing $\mathbf{b}$] are shown in Fig. 6. The first case, $\mathbf{b} = 1.001$ (upper panel of Fig. 6), represents the fixed-boundary limit. It features a singularity (ω_s) located at $\omega_s = 0.4056 v_{A0}/R$ [The value of ω_s is found by applying Newton's method on the function $1/\mathrm{Det}(\hat{L}(\omega))$], which can be shown to be the frequency of the fixed-boundary TAE (the singularity arises as a consequence of the use of basis functions that have finite values at the plasma–vacuum interface, which causes a frequency that would produce a zero displacement at this interface to produce a divergence of $\mathrm{Det}[\hat{L}(\omega)]$ [c.f. Eq. (17)]). Thus, in the case of $\mathbf{b} = 1.001$, the eigenvalue root is adjacent to the singular root, as expected. We concluded that, with quite small $(\mathbf{b} - 1)$ values, the effects due to free-boundary conditions in this particular equilibrium are indeed negligible and the AEGIS code is indeed suitable for obtaining results which are essentially equivalent to that from a fixed plasma boundary calculation. The calculation of $\mathrm{Det}[\hat{L}(\omega)]$ with $\mathbf{b} = 1.2$ is shown in the middle panel of Fig. 6. While the singularity remains at the same frequency (as it should be), the total number of roots has increased from *one* to *two*. The root near the lower continuum tip (which is the lowest value of frequency on the x-axis) is related to the root found in the previous case of $\mathbf{b} = 1.001$, as they both belong to the lower-branch TAE. However, the higher frequency root (which belongs to the upper-branch free-boundary TAE) has no counterpart in the fixed-boundary case as previously concluded.

The results of the calculation with $\mathbf{b} = 2.0$ is shown in the lower panel of Fig. 6. It shows *only one* root located above ω_s, which is an upper-branch free-boundary TAE. The root that is related to the fixed-boundary TAE (i.e., the lower-branch free-boundary TAE) has submerged into the Alfvén continuum and is absent from the frequency gap.

It is illustrative to calculate δW_p, δW_v, and I of the eigenmodes individually using Eqs. (7) and (23) [rather than evaluating $\delta W_p - \omega^2 I$ as a whole, using Eq. (19)] because in view of the variational principle, one may attribute the eigenfrequency into a plasma contribution and a vacuum contribution,

$$\delta W_p + \delta W_v - \omega^2 I = 0$$
$$\Rightarrow \omega^2 = \frac{\delta W_p}{I} + \frac{\delta W_v}{I}.$$

Evaluating $\delta W_p/I$ and $\delta W_v/I$ as a function of $\mathbf{b}$ (Fig. 7), we found that $\delta W_p/I$ decreases and $\delta W_v/I$ increases with increasing $\mathbf{b}$. For all cases, δW_v is at most 5% of δW_p. Therefore, it is the plasma potential energy, rather than the magnetic field energy in vacuum that appears to dominate. However, one cannot rule out the possibility that an effective wall mode is serving as a catalyst for the frequency shift.

B. Plasma pressure (β) study

It was shown in Refs. 12 and 22 that an increase of β decreases the fixed-boundary TAE frequency. In this subsection, we study the relation between β and mode frequency for the free-boundary case. A recessed wall is likely the more relevant boundary condition for fusion reactors which are designed to work in high-β regimes without conducting walls nearby.

We choose $\mathbf{b}$ to be 1.2 and investigate how the increment of β affects the free-boundary TAE. In Fig. 8, we have

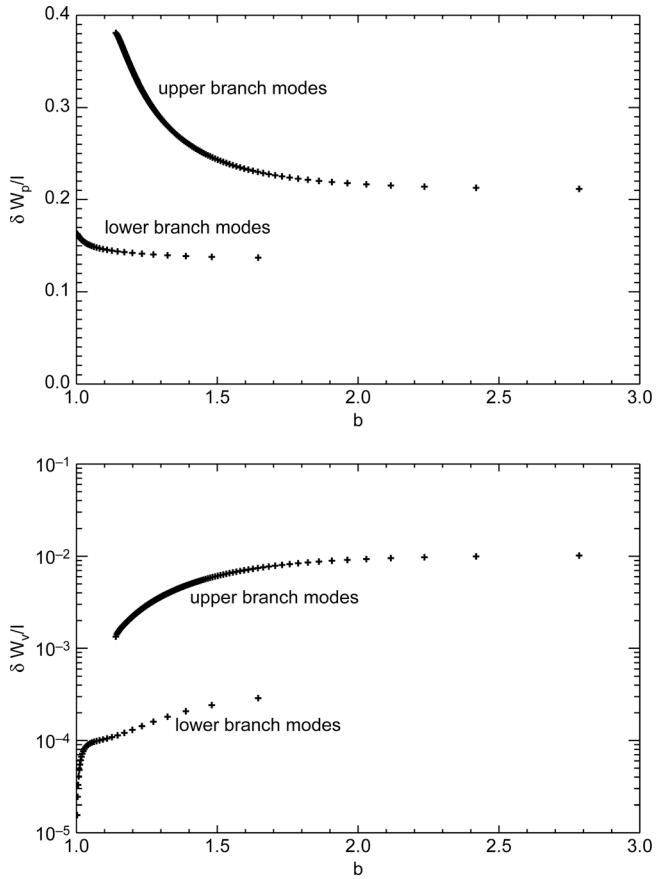

FIG. 7. Upper panel: Normalized plasma potential energy ($\delta W_p/I$) as a function of **b**. Lower panel: Normalized vacuum energy ($\delta W_v/I$) as a function of **b**.

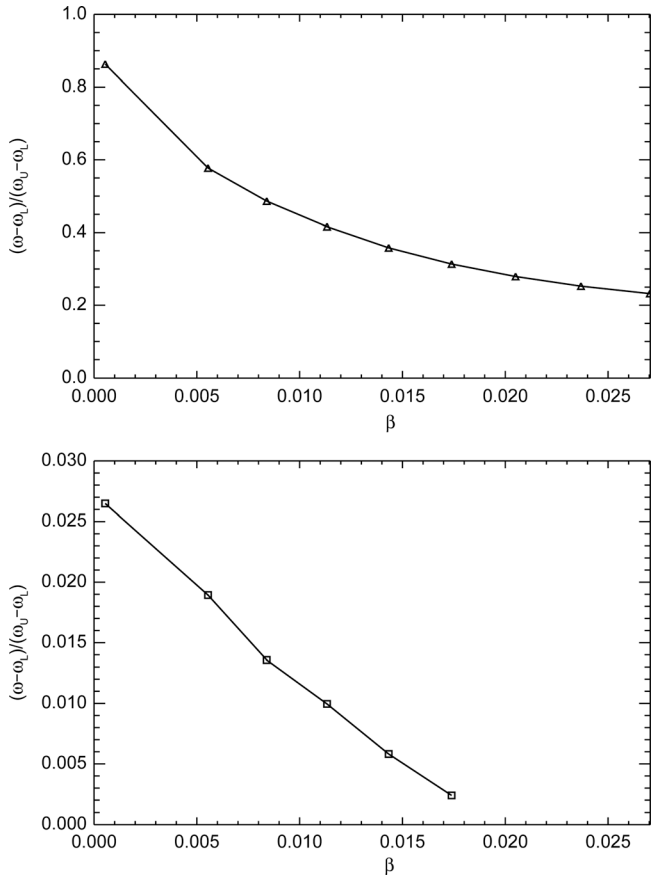

FIG. 8. The relation between β and the frequencies (normalized to continuum gap width) of free-boundary TAE for $\mathbf{b} = 1.2$. The y-values are defined as $(\omega - \omega_L)/(\omega_U - \omega_L)$, with ω_U and ω_L the upper and lower frequency limits of the TAE gap. The upper and lower panels are for the upper and lower branches, respectively.

plotted the relation between β and the frequencies (normalized to continuum gap width) for the upper-branch free-boundary TAE (upper panel) and the lower-branch free-boundary TAE (lower panel) with $\mathbf{b} = 1.2$.

At low β, both the upper-branch and lower-branch modes are present. We found that the frequencies of both modes move downwards as β increases. However, the lower-branch mode (lower panel) enters the lower continuum at a fairly low β ($\sim 1.7\%$). On the other hand, the upper-branch mode (upper panel) does not leave the Alfvén continuum gap even at the highest β we have investigated.

Hence, with sufficient plasma pressure, the upper-branch free-boundary TAE (i.e., the one that does not appear in the fixed-boundary calculation of this equilibrium) is the only observable Alfvén eigenmode in the frequency gap at $\mathbf{b} = 1.2$. This indicates the importance to use the free-boundary conditions for the sake of obtaining *qualitative* insight into the nature of the excited TAE structure.

C. Edge safety factor (q_a) study

In this subsection, we examine the response of free-boundary TAE to a systematic change of q_a, with other plasma parameters (e.g., density profile, β profile and q_0) kept constant.

We consider a total of ten equilibria, in which current profile is changed successively to produce a series of q_a ranging from 2.10 to 2.55. In other words, the q-profile of the equilibrium (upper panel of Fig. 9) goes from the solid line to the dotted line continuously, so is their Alfvén continuum (lower panel of Fig. 9). We then investigate the ω–**b** relation in the fashion of Sec. III A.

We found the basic characteristics of ω–**b** relation at fixed q_a, i.e., the two-branch picture similar to Fig. 3, remains unchanged. The shape of the lines are changed due to the changes made on the equilibrium (upper panel of Fig. 10); however, one can still see a similar pattern formed by the four marked frequencies (U1, U2, L1, L2) of Fig. 3. Looking at the mode structures, we found

(1) The mode structure corresponding to L1 remains similar for different q_a values (c.f. upper panel of Fig. 4).
(2) The mode structure corresponding to L2 always features a strong in-phase $m = 1, 2$ couplet structure around $q = 1.5$, reflecting the fact that it is near the $m = 1, 2$ lower continuum tip. However, the overall global structure (e.g., the structure of $m = 3$ harmonics and the amplitude of $m = 2$ component at the plasma–vacuum interface) is dependent on q_a. For illustration, we have plotted the mode structure in the case of $q_a = 2.1$ and $q_a = 2.55$ in the upper panel and middle panel of Fig. 11.
(3) The mode structure of U1 changes significantly as q_a varies. At lower values of q_a, it features a strong out-of-phase $m = 1, 2$ couplet structure (c.f. upper panel of

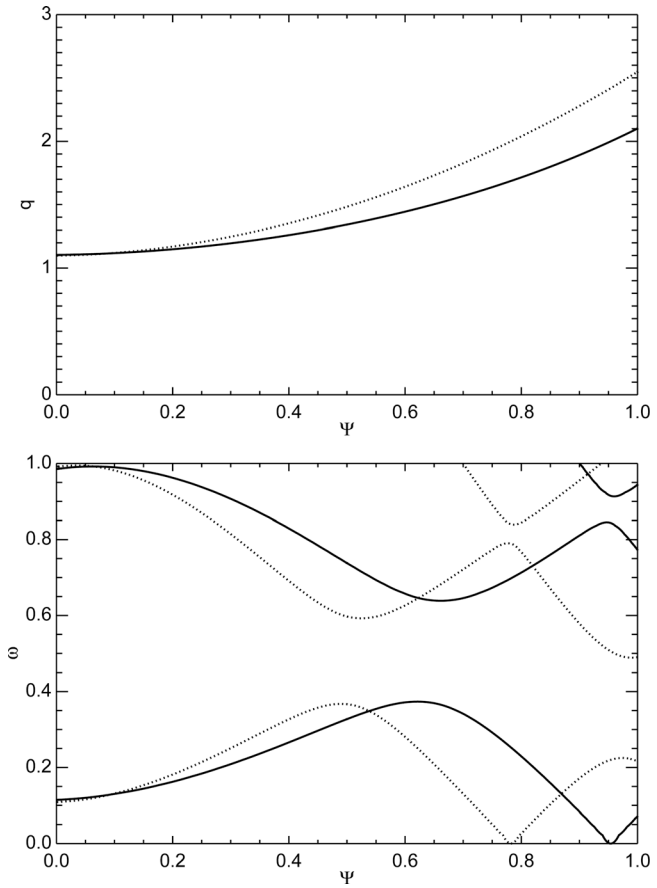

FIG. 9. q-profile (upper panel) and Alfvén continuum (lower panel) for the study of frequency sensitivity to q_a ($2.1 < q_a < 2.55$) and ratio of wall radius to plasma radius.

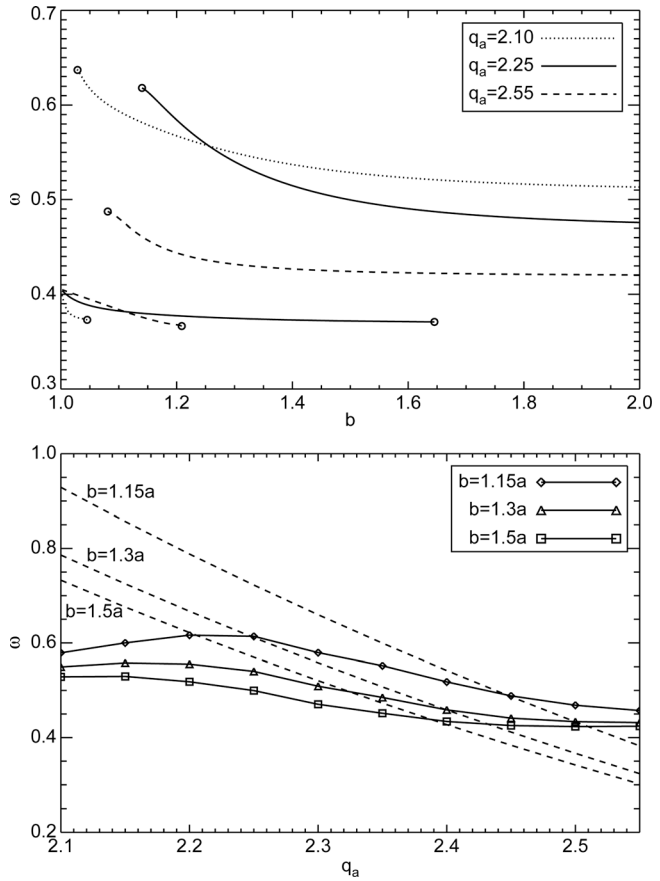

FIG. 10. Study of frequency sensitivity to q_a ($2.1 < q_a < 2.55$) and ratio of wall radius to plasma radius. Upper panel: The ω–**b** relation of free-boundary TAE for three different values of q_a. The hollow circles mark where the modes terminate at upper or lower continuum. Lower panel: ω–q_a relation of the upper-branch free-boundary TAE (solid curves) compared with frequency of model Alfvén surface wave [dashed curves, c.f. Eq. (B8)] for three different wall positions.

Fig. 5) while at higher values of q_a it features a strong out-of-phase $m = 2, 3$ couplet structure (the mode structure in the case of $q_a = 2.55$ is plotted in the lower panel of Fig. 11). This reflects the upper boundary of the gap has changed from $m = 1, 2$ continuum tip to $m = 2, 3$ continuum tip.

(4) The broad mode structure of U2 remains similar as q_a changes (c.f. lower panel of Fig. 5); however, the relative amplitudes for the different harmonics are dependent on q_a.

The presence of a pronounced $m = 3$ component at the plasma–vacuum interface of U2 (c.f. lower panel of Fig. 5) and the ω–**b** relation of the upper free-boundary TAE (c.f. upper panel of Fig. 10) motivate us to compare the predicted frequency of a cylindrical $m = 3$ Alfvén surface wave[23] to the frequency of the upper-branch free-boundary TAE. Therefore, we plot the ω–q_a relation of the $(n, m) = (1, 3)$ Alfvén surface wave (c.f. Appendix B) with that of the upper-branch free-boundary TAE at three different wall positions: $b = 1.15, 1.3, 1.5$ in the lower panel of Fig. 10. We see that there is a correlation of the TAE frequency as a function of **b** and q_a with the frequency predicted for the cylindrical Alfvén surface wave. Thus, there may be a mixing of TAE and $m = 3$ surface modes in determining the frequency of the final eigenmode. Nonetheless, this observation is qualitative, and the correlation might still be arising fortuitously, as other parameters vary as well, e.g., the coupling with additional TAE couplets arising from the $m = 3$ interaction emerging from the edge. If the surface mode is indeed relevant, we find it surprising that the perturbed vacuum potential energies found in Fig. 7 are such a small fraction of the total mode energy.

IV. ALCATOR C-MOD CROSS SECTION

In this section, we would like to show that the sensitivity of TAE to wall position is not only important for systems with low edge q and circular cross section. The free-boundary conditions can have significant impacts on systems with more complex equilibrium as well. For our purposes, we have constructed a plasma model profile similar to that found in Alcator C-Mod. We have adopted the C-Mod geometrical parameters (c.f. upper panel of Fig. 12) with $q_0 = 1.11$, $q_a = 6.28$, and $\beta = 5.76 \times 10^{-3}$. The $n = 1$ Alfvén gap is plotted in the lower panel of Fig. 12, in which a reasonably large fraction of the gap is shown to be in the "shadow" of the continuum. Thus, the frequency domain, where undamped modes can arise, lies between the two horizontal dotted lines in the figure.

We investigate the frequency of the modes in this frequency domain as a function of **b**. Two branches of the

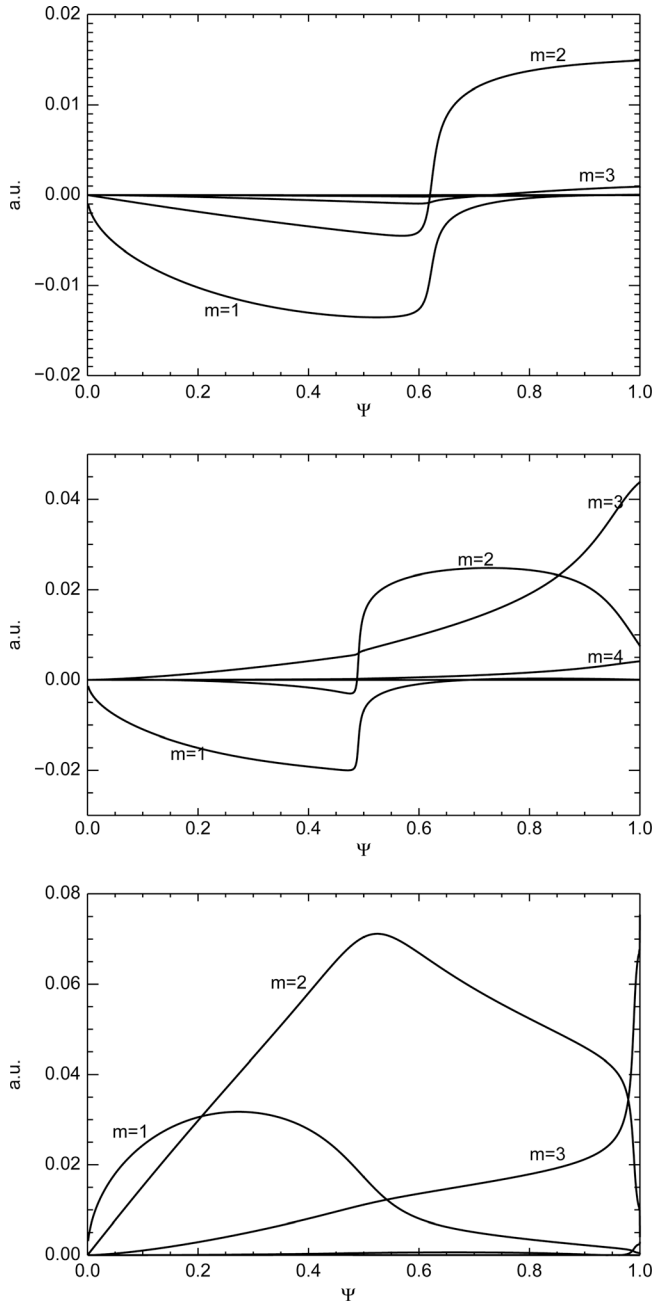

FIG. 11. Three different examples of mode structures (in PEST coordinates) found in q_a scan. Upper panel: Mode structure of L2 for $q_a = 2.10$. Middle panel: Mode structure of L2 for $q_a = 2.55$. Lower panel: Mode structure of U1 for $q_a = 2.55$.

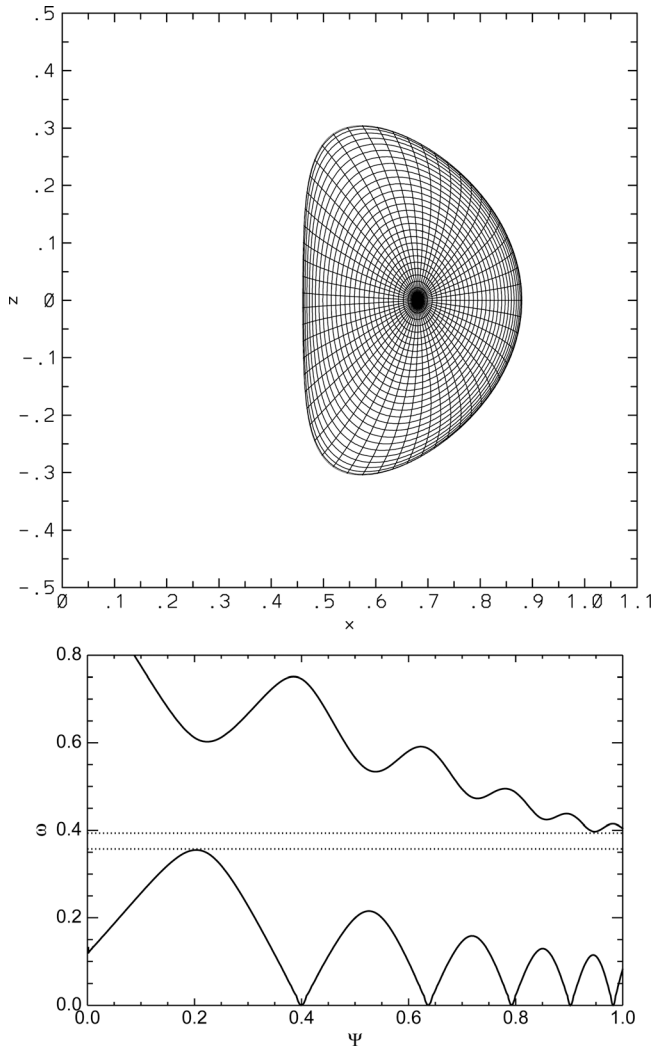

FIG. 12. Model for Alcator C-Mod calculation. Upper panel: Cross section of Alcator C-Mod plasma: $a = 21$cm, $R = 67$ cm, $\kappa_{95} = 1.39$, $\delta_{95} = 0.364$. Lower panel: Alfvén continuum for MHD equilibrium with $\beta = 5.76 \times 10^{-3}$, $q_0 = 1.11$, and $q_a = 6.28$.

undamped free-boundary TAE are found and plotted in Fig. 13. It is noteworthy that the frequency tracking of the upper-branch modes disappears when the frequency intersects the upper continuum at $\mathbf{b} = 1.02$. As the intersecting frequency still lies within the frequency gap of this particular equilibrium, the "lost" mode is expected to be present as a continuum-damped mode, rather than to disappear altogether, as in the case of Sec. III A. However, further work, beyond the scope of the present paper, is required to determine the damping rate and spatial characters.

In Fig. 14, we plot the mode structure at $\mathbf{b} = 1.06$ as this wall position is applicable to some of the C-Mod discharges.[19] In this example, we note that a fixed-boundary calculation would not capture the existence of the undamped TAE of higher frequency. Besides, we found from the plots that the mode amplitude at the outer part of the plasma appears to be a crucial part of the C-Mod TAE structure. The nonvanishing radial perturbations, found with the wall conductor displaced from the plasma, causes significant changes of mode frequency (indicated by Fig. 13) as **b** approach towards unity. We observe from the shape of the eigenmodes that a driving source in the center of the plasma (e.g., energetic particles) could produce a relatively strong excitation at the plasma edge. Therefore, it is important to accurately take the presence and width of vacuum gap into account when analyzing TAE in equilibria which are similar to that found in experiments.

V. CONCLUSION

In this study, we have investigated the global eigenmodes in a TAE gap, taking the effects of the free-boundary conditions into account. We found that in the cases studied, if we start the configuration at $\mathbf{b} = 1$ and then increase **b**, an

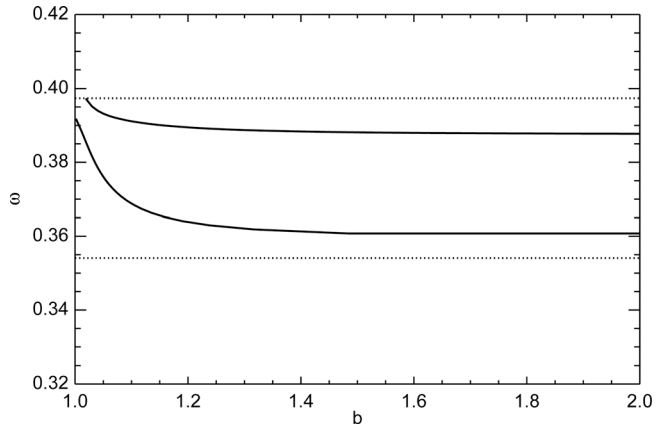

FIG. 13. The ω–**b** relation in the C-Mod like equilibrium.

additional mode generally emerges from the upper continuum when the wall position recedes sufficiently far from the plasma–vacuum boundary. This new mode branch together with the original mode branch share the common feature of generally decreasing in frequency with increasing **b**. What we unexpectedly found is that frequently the original branch is lost to the lower continuum at high enough **b** while the new branch, emerging from the continuum, asymptotes to a constant value within the continuum gap with increasing **b**. The

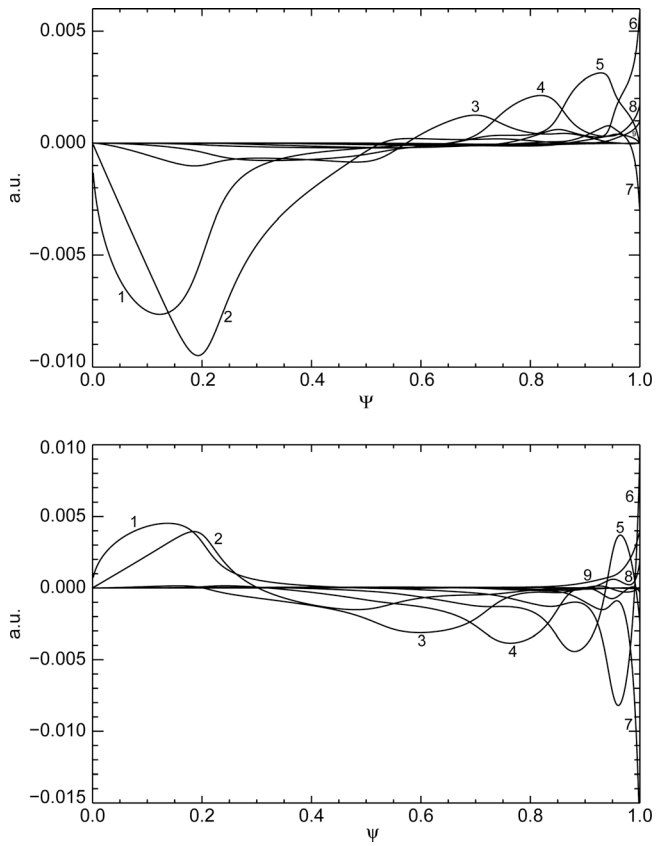

FIG. 14. The mode structure of the free-boundary TAE of C-Mod like equilibrium with **b** = 1.06. The upper panel presents the higher-frequency mode while the lower panel presents the lower-frequency mode. Poloidal numbers are marked alongside the curves. The mode structures are plotted in PEST coordinates.

disappearance of modes was also observed in β scans, a result widely discussed in fixed-boundary cases.[12,22] We have demonstrated that, at a moderately close wall position (**b** = 1.2) and a moderate value of β ($< 2\%$), the new eigenmode branch is the only observable branch for the equilibrium under consideration. We have attempted to better understand why there is such a strong sensitivity of the eigenmode to the wall position. We have observed a correlation of the eigenmode frequency with the Alfvén surface mode frequency predicted for a plasma in cylindrical geometry. This correlation may be responsible for the free-boundary TAE sensitivity to the wall position. However, we do not observe a significant ratio of vacuum energy excitation to plasma potential energy excitation. Hence, the correlation could be fortuitous. At present, we cannot make a definitive conclusion on this point.

We also noted that the effects of free-boundary conditions can be significant in systems with more complex geometry. In our illustrative equilibrium which is similar to that found in Alcator C-Mod, the total number of undamped modes changes from one to two when a suitable free-boundary condition replaces the fixed-boundary condition.

We expect the boundary effects to be less important in high-n calculations as the mode generally becomes internally localized. Nevertheless, the free-boundary effects may still be essential if the mode frequency obtained with fixed-boundary calculations is very close to the lower boundary of the gap. In such case, it is worthwhile to check with free-boundary calculations whether the mode remains inside the frequency gap.

Finally we emphasize the importance of free-boundary calculation for the quantitative prediction of the TAE frequencies especially in dealing with low-n modes. If the frequency can be altered readily by changing edge conditions, one has the possibility of using external means to change the character and perhaps even the stability of the TAE response in hot plasmas with a substantial energetic particle component.

ACKNOWLEDGMENTS

The authors would like to thank Dr. Joseph Snipes for helpful remarks.

APPENDIX A: EXPRESSIONS OF THE EQUILIBRIUM QUANTITIES

For conciseness, we have left the detailed expression of MHD equilibrium quantities out from section II. We present it here for the interested readers. $2U$ in Eq. (2) is defined as

$$2U = 2\mu_0 P'\kappa_\psi + \frac{\sigma^2 B^2}{|\nabla\psi|^2} + \frac{\chi' g}{X^2}\frac{\partial}{\partial\theta}\left(\frac{\sigma\nabla\psi\cdot\nabla\theta}{|\nabla\psi|^2}\right) + \chi'\frac{\sigma q' g}{qX^2}, \tag{A1}$$

where

$$\sigma = \frac{\mu_0\vec{J}\cdot\vec{B}}{B^2} = -\frac{\mu_0 P' g}{B^2\chi'} - \frac{g'}{\chi'}$$

$$\kappa_\psi = \frac{\mu_0 P'}{B^2} + \frac{1}{2B^2}\frac{B^2}{\psi} + \frac{\chi'^2}{2B^4}\frac{\nabla\psi\cdot\nabla\theta}{X^2}\frac{\partial B^2}{\partial\theta}$$

The $M \times M$ MHD equilibrium matrices in Eq. (7) are defined as

$$\begin{aligned}
\mathcal{A}_p &= \frac{\chi'^3 q}{g}\mathcal{K}_\parallel\langle|\nabla\theta|^2\rangle\mathcal{K}_\parallel + \frac{\chi'\chi''^2 q}{g}\langle|\nabla\psi|^2\rangle + \frac{g(q\chi')'^2}{\chi' q}\mathcal{I} \\
&\quad + \mu_0 P'\frac{q\chi''}{g}\langle X^2\rangle + \mu_0 P'\frac{q\chi'}{g}\left\langle\frac{\partial X^2}{\partial\psi}\right\rangle + g'q'\chi'\mathcal{I} \\
&\quad - i\frac{\chi'^2\chi'' q}{g}(\langle\nabla\psi\cdot\nabla\theta\rangle\mathcal{M} - \mathcal{M}\langle\nabla\psi\cdot\nabla\theta\rangle) \\
\mathcal{B}_p &= \frac{\chi' g}{n^2 q}\mathcal{K}_\parallel\mathcal{K}_\parallel \\
\mathcal{C}_p &= \frac{\chi' g}{q}\mathcal{M}\mathcal{M} + \frac{n^2\chi'^3 q}{g}\langle|\nabla\psi|^2\rangle \\
\mathcal{P}_p &= 0 \\
\mathcal{Q}_p &= \frac{\chi' g}{nq}\mathcal{M}\mathcal{K}_\parallel \\
\mathcal{R}_p &= i\frac{n\chi'^3 q}{g}\langle\nabla\psi\cdot\nabla\theta\rangle\mathcal{K}_\parallel - \mu_0 nP'\frac{\chi' q}{g}\langle X^2\rangle \\
&\quad - \frac{n\chi'^2\chi'' q}{g}\langle|\nabla\psi|^2\rangle - n\chi' q g'\mathcal{I} \\
\mathcal{A}_i &= \frac{\chi'^3 q}{g}\left(\left\langle\frac{1}{B^2}\right\rangle + q^2\left\langle\frac{X^2|\nabla\theta|^2}{B^2}\right\rangle\right) \\
\mathcal{B}_i &= \frac{\chi'^3 q}{n^2 g}\left\langle\frac{X^2|\nabla\psi|^2}{B^2}\right\rangle \\
C_i &= n^2\mathcal{B}_i \\
\mathcal{P}_i &= -i\frac{\chi'^3 q^2}{ng}\left\langle\frac{X^2\nabla\psi\cdot\nabla\theta}{B^2}\right\rangle \\
\mathcal{Q}_i &= n\mathcal{B}_i \\
\mathcal{R}_i &= n\mathcal{P}_i,
\end{aligned}$$

where the angle bracket $\langle\cdots\rangle$ denotes the associated Fourier matrix,

$$\langle\cdots\rangle_{mm'} = \frac{1}{2\pi}\int_{-\pi}^{\pi} d\theta(\ldots)e^{i(m'-m)\theta}.$$

Besides, $\mathcal{I}$ is the identity matrix, $\mathcal{K}_\parallel = (m - nq)\mathcal{I}$ and $\mathcal{M} = m\mathcal{I}$.

The matrices used in the vacuum energy integral [Eq. (20)] are defined as

$$\begin{aligned}
\mathcal{J}_v &= \frac{1}{\nabla\psi_v\times\nabla\theta_v\cdot\nabla\varphi} \\
\mathcal{F}_v &= \langle\mathcal{J}_v|\nabla\psi_v|^2\rangle \\
\mathcal{K}_v &= i\langle\mathcal{J}_v\nabla\psi_v\cdot\nabla\theta_v\rangle\mathcal{M} \\
\mathcal{G}_v &= \mathcal{M}\langle\mathcal{J}_v|\nabla\theta_v|^2\rangle\mathcal{M} + n^2\left\langle\frac{\mathcal{J}_v}{X^2}\right\rangle.
\end{aligned}$$

APPENDIX B: ALFVÉN SURFACE WAVE IN CYLINDRICAL GEOMETRY

Here we investigate the Alfvén surface wave in a cylindrical plasma surrounded by vacuum and enclosed by a perfectly conducting wall. We confine our study to a model where the density and safety factor are constant (at values equal to the plasma edge density and q_a of the equilibria studied in the text), in which the analytic theory is particularly simple. Such modeling appears to provide results that are sufficiently good for qualitative purposes.

In cylindrical geometry, the poloidal harmonics (m) is a good quantum number. It can be shown[24] that the Alfvén waves in a cylinder are described by the following equation:

$$\delta\Phi(r,\theta,z,t) = e^{i(nz/R_0 - m\theta - \omega t)}\Phi_{n,m}(r), \tag{B1}$$

$$\begin{aligned}
&\frac{d}{dr}\left[r^3\left(\frac{\omega^2}{v_A^2} - k_\parallel^2\right)\frac{d}{dr}\frac{\Phi_{n,m}(r)}{r}\right] \\
&\quad + \left(\frac{d}{dr}\frac{\omega^2}{v_A^2}\right)r\Phi_{n,m}(r) - (m^2-1)\left(\frac{\omega^2}{v_A^2} - k_\parallel^2\right)\Phi_{n,m}(r) = 0,
\end{aligned} \tag{B2}$$

$$k_\parallel = \frac{1}{R}\left(n - \frac{m}{q}\right), \tag{B3}$$

where $\Phi_{n,m}(r)$ is the Fourier-decomposed scalar potential. For plasma of constant density and q value, $k_\parallel' = v_A' = 0$. The independent solutions of the above equation are, therefore, $\Phi_{n,m}(r) = r^m$ and $\Phi_{n,m}(r) = \frac{1}{r^m}$.

We note the solutions can be naturally separated into two different regions (plasma region and vacuum region). In the plasma region, the regularity at magnetic axis gives

$$\Phi_{n,m}(r) = \left(\frac{r}{a}\right)^m \quad 0 \le r < a, \tag{B4}$$

in which we pick the conventional normalization such that $\Phi_{n,m}(a) = 1$. Similarly, in the vacuum region, we require $\Phi_{n,m}(r)$ to be continuous at $r = a$ and $\Phi_{n,m}(r) = 0$ at $r = b$. Hence,

$$\Phi_{n,m}(r) = \frac{\left(\frac{b}{r}\right)^m - \left(\frac{r}{b}\right)^m}{\left(\frac{b}{a}\right)^m - \left(\frac{a}{b}\right)^m} \quad a \le r \le b. \tag{B5}$$

Keeping in mind that that v_A in vacuum is taken to be infinite, we integrate Eq. (B2) from $r = a^-$ to $r = a^+$ and obtain

$$\left(k_\parallel^2 - \frac{\omega^2}{v_A^2}\right)\frac{d}{dr}\left(\frac{\Phi_{n,m}}{r}\right)_{r=a^-} - \left(\frac{\omega^2\Phi_{n,m}}{v_A^2 r^2}\right)_{r=a^-} = k_\parallel^2\frac{d}{dr}\left(\frac{\Phi_{n,m}}{r}\right)_{r=a^+}. \tag{B6}$$

Using Eqs. (B4)–(B6), we have

$$\omega^2 = \frac{1}{m}\left[(m-1) + \frac{(m+1)\left(\frac{b}{a}\right)^m + (m-1)\left(\frac{a}{b}\right)^m}{\left(\frac{b}{a}\right)^m - \left(\frac{a}{b}\right)^m}\right]k_\parallel^2 v_A^2, \tag{B7}$$

$$\begin{aligned}
&= \frac{1}{m}\left[(m-1) + \frac{(m+1)\left(\frac{b}{a}\right)^m + (m-1)\left(\frac{a}{b}\right)^m}{\left(\frac{b}{a}\right)^m - \left(\frac{a}{b}\right)^m}\right] \\
&\quad \times \left[\frac{B^2}{R_0^2\mu_0\rho}\left(n - \frac{m}{q}\right)^2\right]_{\psi=\psi_a}
\end{aligned} \tag{B8}$$

[1]G. Vlad, F. Zonca, and S. Briguglio, Nuovo Cimento Rivista Serie **22**, 1 (1999).
[2]Y. Nishimura, Phys. Plasmas **16**, 030702 (2009).
[3]S. Hu and L. Chen, Plasma Phys. Controlled Fusion **47**, 1251 (2005).
[4]B. N. Breizman, H. L. Berk, M. S. Pekker, S. D. Pinches, and S. E. Sharapov, Phys. Plasmas **10**, 3649 (2003).
[5]N. N. Gorelenkov, C. Z. Cheng, and G. Y. Fu, Phys. Plasmas **6**, 2802 (1999).
[6]Y. Chen, R. B. White, G. Fu, and R. Nazikian, Phys. Plasmas **6**, 226 (1999).
[7]Y. Kusama, H. Kimura, T. Ozeki, M. Saigusa, G. J. Kramer, T. Oikawa, S. Moriyama, M. Nemoto, T. Fujita, K. Tobita, G. Y. Fu, R. Nazikian, and C. Z. Cheng, Nucl. Fusion **38**, 1215 (1998).
[8]S. Briguglio, F. Zonca, and G. Vlad, Phys. Plasmas **5**, 3287 (1998).
[9]R. Nazikian, G. Y. Fu, Z. Chang, S. H. Batha, H. Berk, R. V. Budny, Y. Chen, C. Z. Cheng, D. S. Darrow, N. N. Gorelenkov, F. M. Levinton, S. Medley, M. P. Petrov, M. Redi, E. Ruskov, D. A. Spong, R. B. White, and S. J. Zweben, Phys. Plasmas **5**, 1703 (1998).
[10]H. L. Berk, J. W. Van Dam, D. Borba, J. Candy, G. T. A. Huysmans, and S. Sharapov, Phys. Plasmas **2**, 3401 (1995).
[11]G. Y. Fu and W. Park, Phys. Rev. Lett. **74**, 1594 (1995).
[12]S. Poedts, W. Kerner, J. P. Goedbloed, B. Keegan, G. T. A. Huysmans, and E. Schwarz, Plasma Phys. Controlled Fusion **34**, 1397 (1992).
[13]M. N. Rosenbluth, H. L. Berk, J. W. Van Dam, and D. M. Lindberg, Phys. Rev. Lett. **68**, 596 (1992).
[14]I. B. Bernstein, E. A. Frieman, M. D. Kruskal, and R. M. Kulsrud, Proc. R. Soc. London, Ser. A **244**, 17 (1958).
[15]M. S. Chance, J. M. Greene, R. C. Grimm, and J. L. Johnson, Nucl. Fusion **17**, 65 (1977).
[16]B. Balet, K. Appert, and J. Vaclavik, Plasma Phys. **24**, 1005 (1982).
[17]S. Poedts, W. Kerner, and M. Goossens, J. Plasma Phys. **42**, 27 (1989).
[18]W. Kerner, J. Comput. Phys. **142**, 271 (1998).
[19]J. A. Snipes, N. N. Gorelenkov, and J. A. Sears, Nucl. Fusion **46**, 1036 (2006).
[20]L. Zheng and M. Kotschenreuther, J. Comput. Phys. **211**, 748 (2006).
[21]R. C. Grimm, J. M. Greene, and J. L. Johnson, *Methods of Computational Physics* (Academic, New York, 1976), p. 253.
[22]G. Y. Fu and C. Z. Cheng, Phys. Fluids B **2**, 985 (1990).
[23]C. Uberoi and K. Somasundaram, Plasma Phys. **22**, 747 (1980).
[24]H. L. Berk, J. W. Van Dam, Z. Guo, and D. M. Lindberg, Phys. Fluids B **4**, 1806 (1992).